

Article

Effect of TiS₂ on Hydrogen Absorption and Desorption Performance of Mechanically Ball-Milled Mg₉₅Ce₅ Alloy

Haitao Lv ¹, Liangrui Wang ¹, Xiulong Ou ^{1,*} and Zhiming Li ^{1,2}

¹ Center for Research on the Preparation and Properties of New Functional Materials, Hanjiang Normal University, Shiyan 442000, China; wangliangrui@hjnu.edu.cn (L.W.)

² Key Laboratory of Quark and Lepton Physics (MOE) and Institute of Particle Physics, Central China Normal University, Wuhan 430079, China

* Correspondence: ouxiulong@hjnu.edu.cn

Abstract: Magnesium-based materials have been considered to be potential hydrogen storage materials due to their high hydrogen storage capacity and abundance in natural resources. In order to improve the hydrogen storage performance of magnesium-based materials, a Mg₉₅Ce₅ alloy was prepared by using the vacuum induction melting method. Moreover, TiS₂ was used as a catalyst, and a series of Mg₉₅Ce₅ + x wt% TiS₂ ($x = 0, 3, 5$ and 10) composites with different TiS₂ contents were prepared by the mechanical ball-milling method. The addition of TiS₂ as a catalyst broke the inherent symmetry of the Mg₉₅Ce₅ alloy at both the atomic and defect levels, potentially improving hydrogen storage by modifying hydrogen diffusion pathways and interaction sites. The structural analysis results indicate that the Mg₉₅Ce₅ alloy is composed of Mg and CeMg₁₂ phases. After the hydrogenation process, the Mg and CeMg₁₂ phases in the Mg₉₅Ce₅–TiS₂ composites transformed into CeH_{2.73} and MgH₂. In addition, CeS₂ and TiH_{1.5} could be detected in the hydrogenated samples, indicating that the TiS₂ decomposed and changed into CeS₂ and TiH_{1.5} during the hydrogenation reaction. Adding TiS₂ to Mg₉₅Ce₅ alloy could significantly improve the hydrogen absorption and desorption kinetic properties, and the dehydrogenation peak temperature of the composites was reduced from 389.5 °C to 329.7 °C when the TiS₂ content increased from 0 to 10 wt%. However, the addition of TiS₂ inevitably reduced the reversible hydrogen storage capacity of the composites. The hydrogen absorption and desorption thermodynamic measurement results indicate that the TiS₂ catalyst has almost no influence on the enthalpy and entropy changes of the composites during the hydrogenation process.



Academic Editors: Luigi Nicolais and Zine El Abidine Fellah

Received: 10 November 2024

Revised: 15 December 2024

Accepted: 25 December 2024

Published: 4 January 2025

Citation: Lv, H.; Wang, L.; Ou, X.; Li, Z. Effect of TiS₂ on Hydrogen Absorption and Desorption Performance of Mechanically Ball-Milled Mg₉₅Ce₅ Alloy. *Symmetry* **2025**, *17*, 71. <https://doi.org/10.3390/sym17010071>

Copyright: © 2025 by the authors. Licensee MDPI, Basel, Switzerland. This article is an open access article distributed under the terms and conditions of the Creative Commons Attribution (CC BY) license (<https://creativecommons.org/licenses/by/4.0/>).

1. Introduction

The environmental pollution and energy crisis are common challenges that human beings are facing. Moreover, the greenhouse effect resulting from the use of fossil fuels is an important problem in the development of society. Creating technology that converts carbon dioxide into valuable products is an attractive way to reduce the greenhouse effect [1,2]. More importantly, it is necessary to develop renewable energy to entirely solve the energy problem. Hydrogen energy is recognized as one of the ideal secondary energy sources due to its non-toxicity, non-polluting nature, high energy density, and renewability [3]. However, efficient and safe hydrogen storage technology still sets a strict limit on the development of the utilization of hydrogen energy [4]. Magnesium and its hydride are recognized as the optimal solid hydrogen storage material due to their high storage density of up to 7.6 wt%,

good reversibility, and low cost [5]. However, the high decomposition temperature and slow reaction kinetics of Mg/MgH₂ significantly limit its practical applications [6].

To address these challenges, various methods have been explored to improve the hydrogen storage performance of magnesium-based materials, such as alloying with other elements [7–9], doping catalysts [10–12], nanosizing [13–15], and so on. In materials science, it is known that symmetry plays a key role in hydrogen absorption and desorption in alloys, as it affects structural stability, atomic arrangements, and phase transitions. The alloying method consists of adding other elements to magnesium by alloy smelting to obtain alloys, thus enhancing the hydrogen storage performance of magnesium. Xie et al. [16] prepared Mg-Ce alloys with various Ce contents, and the phase compositions, micro-structures, and hydrogen storage performance of the alloys were investigated. They found that the addition of Ce significantly improves the hydrogen absorption kinetic properties of the alloy, and the dehydrogenation temperature can be obviously reduced with the increase of Ce content. Yang et al. [17] prepared several Mg₂₄Y₃M (M = Ni, Co, Cu, Al) ternary alloys, and the research results indicate that the alloy with different chemical components showed significantly different features in its microstructure and hydrogen storage properties. Mg₂₄Y₃Ni had the best hydrogen absorption and desorption kinetic performance. Doping catalysts is also an effective method to improve the hydrogen storage kinetic properties of Mg/MgH₂ [18]. Currently, the catalysts used for hydrogen storage materials mainly include metals and alloys [19,20], oxides [21,22], halides [23,24], carbide [11], and carbonaceous materials [25]. The addition of transition metal elements or their inorganic compounds has proven to be an effective method for enhancing the hydrogen storage performance of magnesium-based materials. Oelerich et al. [26] doped different transition metallic oxides (Sc₂O₃, TiO₂, V₂O₅, Cr₂O₃, Mn₂O₃, Fe₃O₄, CuO/Al₂O₃, and SiO₂) into MgH₂ by a simple ball-milling method, and the hydrogen storage measurement results indicate that all these oxide catalysts can improve the hydrogen absorption and desorption performance of MgH₂. Li et al. [27] synthesized a nanocrystalline Ni@C composite using a self-templating method and then doped it into MgH₂ to investigate its catalytic impact on the hydrogen storage properties of MgH₂. The research results demonstrate that the dehydrogenation temperature of the composite was lowered by more than 74 °C compared to pure MgH₂.

In recent years, metal sulfides have aroused more attention due to their outstanding catalytic properties the in water-electrolytic hydrogen evolution and photocatalytic fields [28,29]. Moreover, metal sulfides also have unique catalytic effects in improving the hydrogen storage performance of magnesium-based materials. Yuan et al. [30–32] compared the catalytic effects of CoS₂ and MoS₂ nano-particles on the hydrogen storage properties of Sm-Mg binary alloy. They found that both of the sulfides could obviously improve the hydrogenation and dehydrogenation kinetics of Sm-Mg alloy, and the composite catalyzed by MoS₂ exhibits better hydrogen storage properties. Wang et al. [33] also synthesized NiS₂ particles by a one-step hydrothermal method, and various MgH₂-NiS₂ composites with different NiS₂ contents were prepared by mechanical ball-milling. The study indicates that the NiS₂ decomposed and transformed into MgS and Mg₂NiH₄ phases during the hydrogenation process, and the catalytic phases formed *in situ* significantly improved the hydrogenation and dehydrogenation kinetic properties of MgH₂. Based on previous studies, a Mg₉₅Ce₅ alloy was prepared by using the vacuum induction melting method in this study. Then TiS₂ was selected as a catalyst to dope into Mg₉₅Ce₅ alloy by using the mechanical ball-milling method to prepare a series of Mg₉₅Ce_{5-x} wt% TiS₂ ($x = 0, 3, 5$ and 10) composites with different TiS₂ contents. The effects of TiS₂ content on microstructure and hydrogen storage properties of Mg₉₅Ce₅-TiS₂ composites were studied,

and the catalytic mechanism of the TiS_2 on hydrogen absorption and desorption reactions of $\text{Mg}_{95}\text{Ce}_5$ alloy was investigated in detail.

2. Experimental Details

2.1. Material Preparation

$\text{Mg}_{95}\text{Ce}_5$ alloy was prepared by the vacuum induction melting method using pure magnesium and cerium as the raw materials. A magnesia crucible with 30 mm in diameter and 70 mm in height was used to melt the alloy. The pre-weighed magnesium and cerium were added to the crucible, and the total weight of the raw materials was approximately 60 g. The whole smelting process was performed under argon protection. The raw materials were heated by a high-frequency induction power source. After complete melting of the metal blocks, the molten alloy was cooled to room temperature to form a cylindrical alloy ingot.

The $\text{Mg}_{95}\text{Ce}_5$ alloy ingot was crushed into alloy particles smaller than 200 mesh using an agate grinder. The TiS_2 powder was purchased from Shanghai Titan Scientific Co. (Shanghai, China). Then $\text{Mg}_{95}\text{Ce}_{5-x}$ wt% TiS_2 ($x = 0, 3, 5$, and 10) composites with different TiS_2 contents were prepared using the mechanical ball-milling technique. The ball-milling process was carried out on a planetary ball-mill in an argon atmosphere, and the total material mass was about 2 g. The ball-to-powder weight ratio was 60:1, the rotational speed was 400 rpm, and the milling time was 5 h. For convenience, the $\text{Mg}_{95}\text{Ce}_{5-x}$ wt% TiS_2 ($x = 0, 3, 5$, and 10) composites with different TiS_2 contents are abbreviated to $\text{Mg}_{95}\text{Ce}_5$, $\text{Mg}_{95}\text{Ce}_5\text{-}3 \text{ TiS}_2$, $\text{Mg}_{95}\text{Ce}_5\text{-}5 \text{ TiS}_2$, and $\text{Mg}_{95}\text{Ce}_5\text{-}10 \text{ TiS}_2$, respectively.

2.2. Structural and Morphological Characterizations

The phase composition of the prepared samples was analyzed using X-ray diffraction (XRD, Bruker D8 Advance, Billerica, MA, USA). During sample transfer and measurement, the samples were sealed with amorphous membranes to avoid exposing them to air. The morphology and microstructure of the samples were examined by scanning electron microscopy (SEM, JSM-7100F, Tokyo, Japan).

2.3. Hydrogen Storage Measurements

The de/re-hydrogenation performance of the samples was tested using a Sieverts-type experimental apparatus. A powder sample weighing about 0.3 g was loaded into a stainless-steel reactor equipped with temperature and pressure sensors. The sample was hydrogenated five times at 380°C to reach a stable hydrogen storage performance, and then the hydrogen absorption and desorption measurements at various temperatures were performed. The hydrogen absorption kinetic tests were performed under a hydrogen pressure of 4 MPa, while the hydrogen desorption kinetic tests were conducted at a hydrogen pressure below 0.03 MPa. The temperature-programmed desorption (TPD) experiments were also carried out in the Sieverts-type apparatus. Before the TPD tests, the samples were hydrogenated at 380°C at 3 MPa and then cooled down to room temperature to obtain fully hydrogenated samples. Then the fully hydrogenated samples were heated from room temperature up to 500°C at a heating rate of 3°C min^{-1} to obtain TPD curves. The pressure–composition isotherm (p - c - T) curves at various temperatures were tested by gradually increasing hydrogen pressure to 4 MPa and followed by decreasing hydrogen pressure to below 0.02 MPa.

3. Results and Discussion

The phase compositions and microtopography features of the TiS_2 catalyst and $\text{Mg}_{95}\text{Ce}_5$ alloy were characterized using XRD and SEM analysis, and the results are il-

lustrated in Figure 1. It can be observed in Figure 1a that the TiS_2 sample exhibits distinct diffraction peaks, indicating it is a typical crystalline structure. Figure 1b presents the SEM image of TiS_2 powder. It can be seen that the TiS_2 particles exhibit a polygonal flake-like structure and particle size of 5~20 μm . The XRD analysis results in Figure 1a indicate that the $\text{Mg}_{95}\text{Ce}_5$ alloy is composed of CeMg_{12} and Mg phases, and the sharp diffraction peaks imply the alloy has good crystallinity. Figure 1c shows the SEM image (backscattered electron image) of the $\text{Mg}_{95}\text{Ce}_5$ alloy ingot. It is evident that the alloy mainly consists of two structures: the one is a coarse and gray-white blocky phase (marked A), and the other is a eutectic structure composed of a striped or globular gray-white phase and a black phase (marked B). In general, elements with bigger atomic numbers appear brighter in backscattered electron images. Combined with XRD analysis and a Mg–Ce binary phase diagram [34], we can conclude that the gray-white phase in areas A and B is CeMg_{12} , and the black phase in area B is Mg.

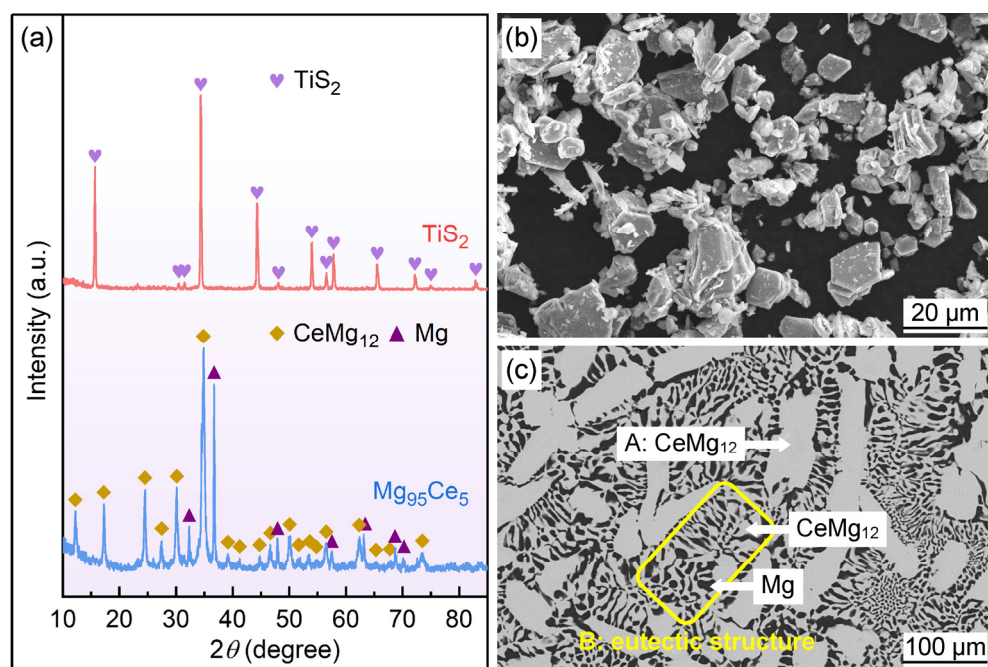


Figure 1. XRD patterns and SEM images of the TiS_2 catalyst and the $\text{Mg}_{95}\text{Ce}_5$ alloy: (a) XRD patterns of the TiS_2 and $\text{Mg}_{95}\text{Ce}_5$ samples; (b) SEM image (secondary electron image) of the TiS_2 catalyst; (c) SEM image (backscattered electron image) of the $\text{Mg}_{95}\text{Ce}_5$ alloy ingot.

$\text{Mg}_{95}\text{Ce}_5$ – TiS_2 composites with different TiS_2 content were prepared by the mechanical ball-milling method, and the XRD patterns of the composites are shown in Figure 2. It can be observed that the ball-milling process has almost no influence on the phase compositions of the alloy, and the ball-milled $\text{Mg}_{95}\text{Ce}_5$ alloy still consists of CeMg_{12} and Mg phases. However, the diffraction peaks of the ball-milled $\text{Mg}_{95}\text{Ce}_5$ alloy are broadened and weakened, which can be attributed to the lattice distortion and grain refinement resulted from the ball-milling process [35]. Moreover, Figure 2 also illustrates that the TiS_2 content has little effect on the phase composition of $\text{Mg}_{95}\text{Ce}_5$ – TiS_2 composites. Meanwhile, the diffraction peaks of TiS_2 cannot be observed in the $\text{Mg}_{95}\text{Ce}_5$ – TiS_2 composites, even when the TiS_2 content reaches 10 wt%. This may be due to the fact that the crystal structure of TiS_2 is destroyed under the high-impact energy in the ball-milling process [36,37].

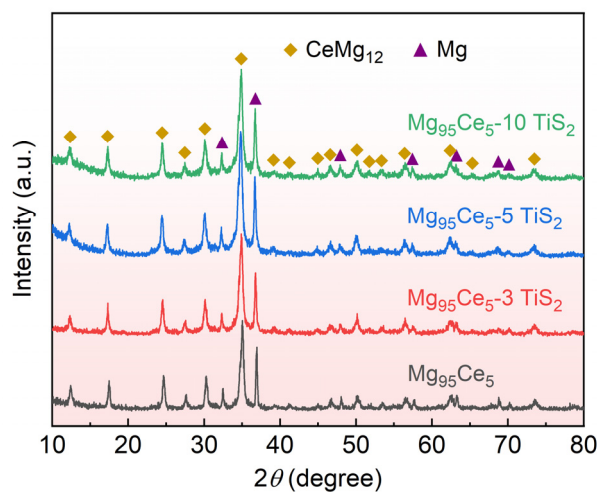


Figure 2. XRD patterns of the ball-milled $\text{Mg}_{95}\text{Ce}_5\text{-TiS}_2$ composites with different TiS_2 contents.

Figure 3 shows the SEM images of the ball-milled $\text{Mg}_{95}\text{Ce}_5\text{-TiS}_2$ composites with different TiS_2 contents. The figure illustrates that these ball-milled composites contain irregular particles with a particle size of 20~50 μm . Increasing TiS_2 content appears slightly reduce the particle size of the alloy powders. This phenomenon may be ascribed to the added grinding effect of the TiS_2 .

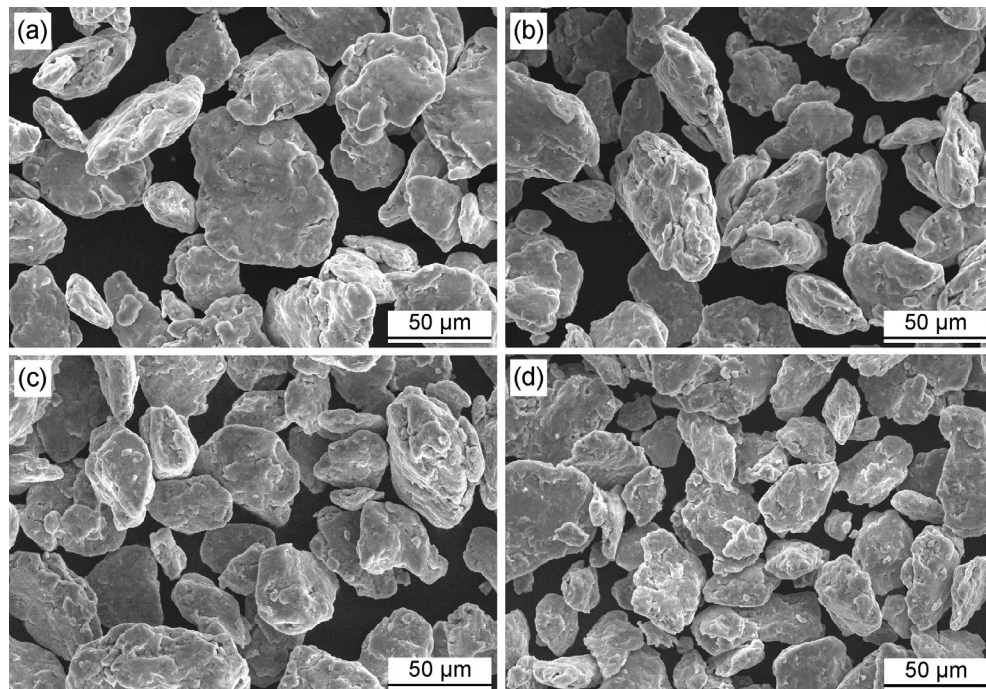


Figure 3. SEM images of the ball-milled $\text{Mg}_{95}\text{Ce}_5\text{-TiS}_2$ composites with different TiS_2 content: (a) $\text{Mg}_{95}\text{Ce}_5$; (b) $\text{Mg}_{95}\text{Ce}_5\text{-}3 \text{ TiS}_2$, (c) $\text{Mg}_{95}\text{Ce}_5\text{-}5 \text{ TiS}_2$, (d) $\text{Mg}_{95}\text{Ce}_5\text{-}10 \text{ TiS}_2$.

To explore the phase transformations of the $\text{Mg}_{95}\text{Ce}_5\text{-TiS}_2$ composites during hydrogenation processes, XRD tests were conducted on the hydrogenated and dehydrogenated composite materials. It can be seen from Figure 4a that the hydrogenated $\text{Mg}_{95}\text{Ce}_5$ sample mainly contained MgH_2 and $\text{CeH}_{2.73}$. Clearly, the CeMg_{12} and Mg phases in the alloy were completely transformed into MgH_2 and $\text{CeH}_{2.73}$ in the hydrogen absorption process. This result is consistent with the hydrogenation process of Mg_3RE (RE represents rare earths) intermetallic compounds [38]. Moreover, the diffraction peaks of CeS_2 and $\text{TiH}_{1.5}$ could be detected in the hydrogenated $\text{Mg}_{95}\text{Ce}_5\text{-TiS}_2$ samples. Therefore, it can be asserted that

the TiS_2 decomposed and transformed in situ into CeS_2 and $\text{TiH}_{1.5}$ during hydrogenation. The appearance of CeS_2 suggests that sulfur is more likely to combine with cerium rather than magnesium to form a CeS_2 compound. Figure 4b shows the XRD patterns of the dehydrogenated $\text{Mg}_{95}\text{Ce}_5\text{-TiS}_2$ composites. The figure shows that the diffraction peaks of MgH_2 disappeared to be replaced by the diffraction peaks of Mg. Obviously, the MgH_2 in hydrogenated samples can be completely decomposed and release hydrogen during dehydrogenation process. Moreover, there is no chemical reaction occurs in the $\text{CeH}_{2.73}$, CeS_2 and $\text{TiH}_{1.5}$ phases during hydrogen absorption and desorption cycles. The $\text{CeH}_{2.73}$ and $\text{TiH}_{1.5}$ has good chemical stability and there is decomposition reaction only at higher temperatures [39,40]. Despite of this, the in-situ formed $\text{CeH}_{2.73}$, CeS_2 and $\text{TiH}_{1.5}$ can dramatically catalyze the hydrogen absorption and desorption reactions.

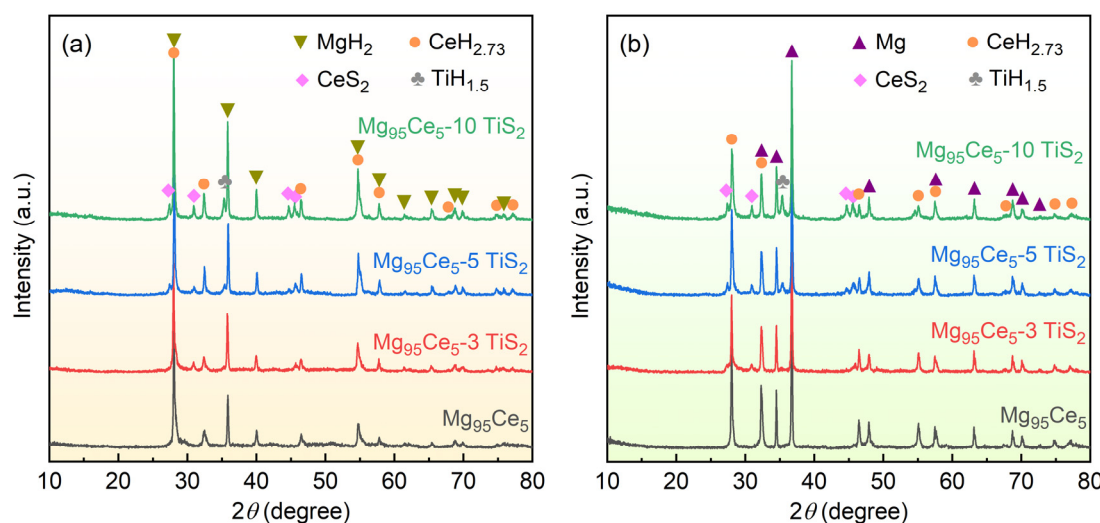


Figure 4. XRD patterns of the hydrogenated and dehydrogenated $\text{Mg}_{95}\text{Ce}_5\text{-TiS}_2$ composites: (a) hydrogenated samples; (b) dehydrogenated samples.

After five hydrogen absorption and desorption cycles, the $\text{Mg}_{95}\text{Ce}_5\text{-TiS}_2$ composites could achieve a stable reaction kinetics. Then the TPD curves, isothermal hydrogen absorption/desorption kinetic curves, and $p\text{-}c\text{-}T$ curves could be measured. Figure 5 exhibits the TPD curves of the composite samples at a heating rate of $3\text{ }^\circ\text{C min}^{-1}$. The dehydrogenation peak temperature of the $\text{Mg}_{95}\text{Ce}_5$ alloy was approximately $389.5\text{ }^\circ\text{C}$, and the entire desorption reaction was completed when the temperature exceeded $450\text{ }^\circ\text{C}$. Notably, the dehydrogenation temperature of the $\text{Mg}_{95}\text{Ce}_5\text{-TiS}_2$ composite material was much lower than that of the $\text{Mg}_{95}\text{Ce}_5$ alloy sample, and the dehydrogenation peak temperature of the materials gradually decreased to $329.7\text{ }^\circ\text{C}$ when the TiS_2 content increased to 10 wt%. However, the addition of TiS_2 increased the total weight of the $\text{Mg}_{95}\text{Ce}_5\text{-TiS}_2$ composites and inevitably reduced its effective hydrogen storage capacity.

Figure 6 presents the hydrogen absorption and desorption curves of the $\text{Mg}_{95}\text{Ce}_5\text{-TiS}_2$ composites at various temperatures. From the hydrogen absorption kinetic curves shown in Figure 6a–c, we can observe that all the samples exhibited good hydrogen absorption kinetics at $380\text{ }^\circ\text{C}$. That is, the TiS_2 catalyst did not have a significant impact on the hydrogen absorption kinetics of the composite at higher temperatures. With the decreases of operating temperature, the hydrogen absorption rate of the pure alloy material began to be limited. For example, the $\text{Mg}_{95}\text{Ce}_5\text{-10 TiS}_2$ composite reached full hydrogenation saturation within 75 min at $250\text{ }^\circ\text{C}$, whereas the $\text{Mg}_{95}\text{Ce}_5$ only reached full saturation at around 300 min. From the hydrogen desorption kinetic curves shown in Figure 6d–f, it can be seen that the hydrogen desorption kinetics of the $\text{Mg}_{95}\text{Ce}_5\text{-TiS}_2$ composites were also much faster than those of the $\text{Mg}_{95}\text{Ce}_5$ alloy. More importantly, increasing TiS_2 content significantly

increased the hydrogen desorption rate. However, the maximal hydrogen absorption and desorption capacities of the composites gradually decreased with the increase of TiS_2 content, which coincided with the results of the TPD test.

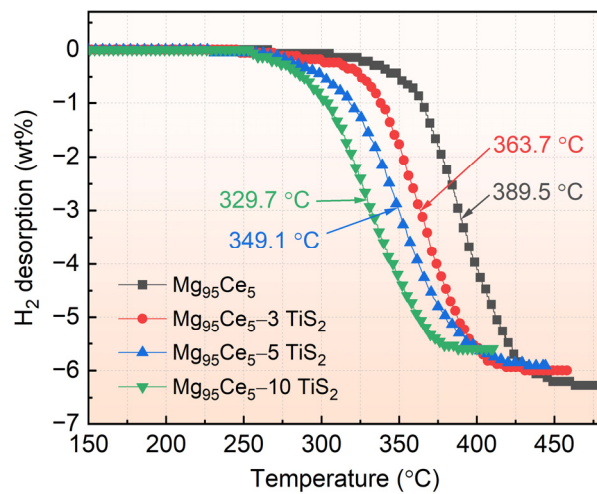


Figure 5. TPD curves of the $\text{Mg}_{95}\text{Ce}_5\text{-TiS}_2$ composites measured at a heating rate of $3 \text{ }^{\circ}\text{C min}^{-1}$.

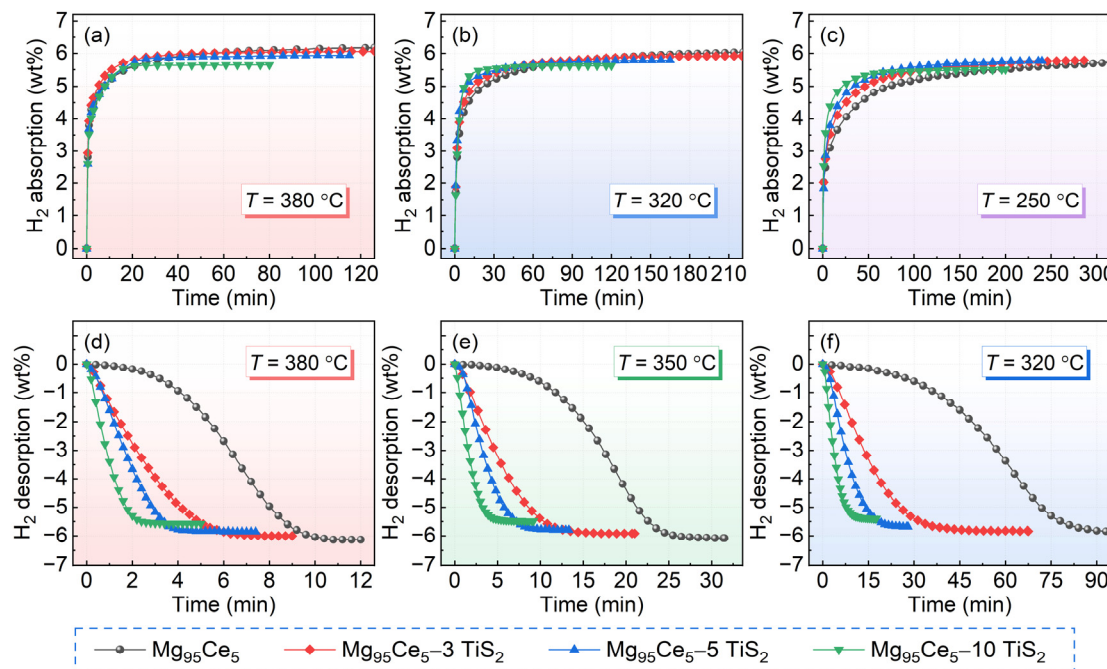


Figure 6. Hydrogen absorption and desorption kinetic curves of the $\text{Mg}_{95}\text{Ce}_5\text{-TiS}_2$ composites at various temperatures: (a–c) absorption curves; (d–f) desorption curves.

Generally, the dehydrogenation reaction of magnesium hydride follows the nucleation growth model [41]. The Johnson–Mehl–Avrami–Kolmogorov (JMAK) formula can be used to fit the dehydrogenation kinetic curves of the $\text{Mg}_{95}\text{Ce}_5\text{-TiS}_2$ composites for a better understanding of the dehydrogenation mechanism. The JMAK formula can be expressed as [42]:

$$\ln[-\ln(1-\alpha)] = n \ln k + n \ln t \quad (1)$$

where α represents the extent of the dehydrogenation reaction at moment t , n denotes the Avrami exponent, and k is the reaction rate constant, which depends on temperature. The kinetic curve of hydrogen desorption at various temperatures was fitted with a linear JMAK equation by plotting $\ln[-\ln(1-\alpha)]$ against $\ln t$. In this plot, n corresponds to

the fitting slope, while $n\ln k$ is the intercept. The JMAK fitting results are illustrated in Figure 7a–d, where a clear linear relationship is observed in each plot, indicating that the dehydrogenation reaction of the Mg₉₅Ce₅–TiS₂ composite material conforms to the JMAK model. The calculated values of n and $\ln k$ are presented in Table 1. The values of n for the ball-milled Mg₉₅Ce₅ alloy range from 3.305 to 3.696, suggesting that three-dimensional interfacial growth determines the dehydrogenation process [19]. After doping with TiS₂, the Avrami coefficients of the samples varied from 1.341 to 1.788, implying that the dehydrogenation process of the TiS₂-catalyzed Mg₉₅Ce₅–TiS₂ composites could be described using a zero-nucleation rate mechanism and the reaction was limited by the one-dimensional diffusion of the elements [27]. It is obvious that the CeH_{2.73}, CeS₂, and TiH_{1.5} formed in situ play the role of nucleating agents during the dehydrogenation process of the Mg₉₅Ce₅–TiS₂ composites and significantly accelerate the hydrogen desorption kinetic performance of MgH₂ in the composites.

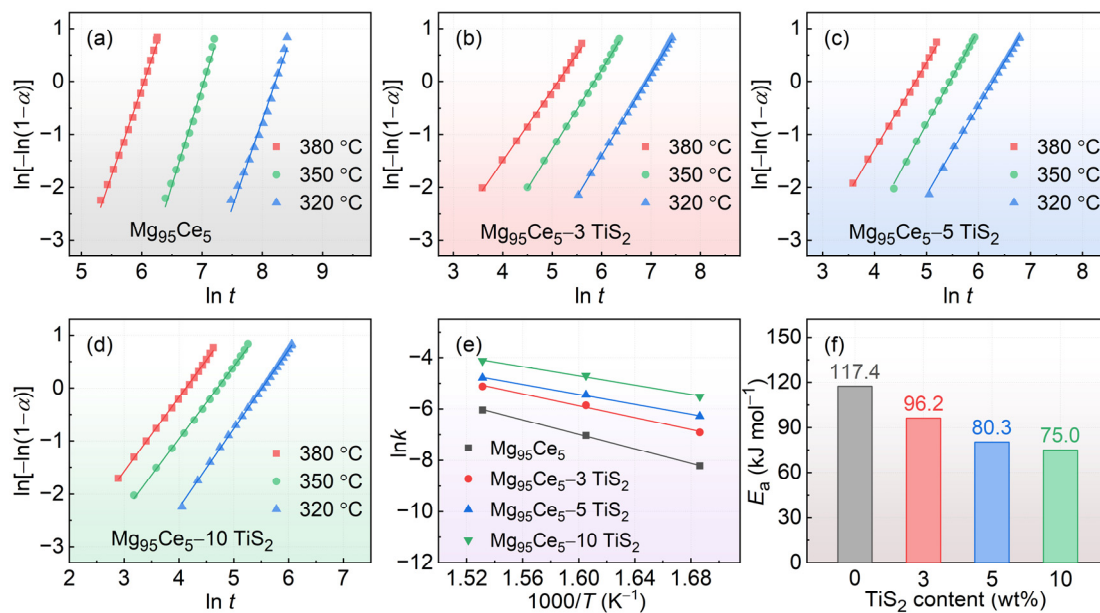


Figure 7. (a–d) JMAK fitting results of $\ln[-\ln(1-\alpha)]$ versus $\ln t$ and corresponding fitting lines for the dehydrogenation of Mg₉₅Ce₅–TiS₂ composites; (e) Arrhenius plots and corresponding fitting lines for the composites; (f) obtained E_a values of the composites with different TiS₂ contents.

Table 1. JMAK fitting results of the Mg₉₅Ce₅–TiS₂ composites.

Samples	n			$\ln k$		
	320 °C	350 °C	380 °C	320 °C	350 °C	380 °C
Mg ₉₅ Ce ₅	3.315	3.696	3.305	-8.220	-7.031	-6.036
Mg ₉₅ Ce ₅ –3 TiS ₂	1.544	1.494	1.341	-6.908	-5.853	-5.120
Mg ₉₅ Ce ₅ –5 TiS ₂	1.688	1.788	1.636	-6.279	-5.450	-4.784
Mg ₉₅ Ce ₅ –10 TiS ₂	1.487	1.369	1.403	-5.514	-4.670	-4.120

The dehydrogenation kinetic performance is typically characterized by the apparent dehydrogenation activation energy (E_a), which can be calculated using the Arrhenius equation [43]:

$$\ln k = -\frac{E_a}{RT} + \ln k_0 \quad (2)$$

where $\ln k$ can be determined from Equation (1), E_a represents the apparent dehydrogenation activation energy (kJ mol⁻¹), R denotes the molar gas constant (8.314 J mol⁻¹ K⁻¹), T is the thermodynamic temperature in Kelvin, and k_0 is a constant. Figure 7e illustrates the

Arrhenius fitting curves of $\ln k$ plotted against $1000/T$. The E_a values can be derived from the slope of the fitted lines, and these obtained values are also compared in Figure 7f. We notice that the E_a value for dehydrogenation reactions decreased from $117.4 \text{ kJ mol}^{-1}$ to 75.0 kJ mol^{-1} with the increase of TiS_2 content from 0 to 10 wt%. The E_a value of the $\text{Mg}_{95}\text{Ce}_5\text{-TiS}_2$ sample in this study was much lower than that of the $\text{MgH}_2/\text{TiO}_2$ composites ($106.7 \text{ kJ mol}^{-1}$) [44] and $\text{MgH}_2\text{-Ni/TCN}$ material (82.6 kJ mol^{-1}) [45] reported before. Therefore, we can conclude that adding TiS_2 to $\text{Mg}_{95}\text{Ce}_5$ alloy can obviously decrease the dehydrogenation activation energy and therefore significantly improves the hydrogen desorption kinetic performance of the alloy.

To further investigate the impact of TiS_2 on the hydrogen storage thermodynamics of the $\text{Mg}_{95}\text{Ce}_5$ alloy, the $p\text{-}c\text{-}T$ curves of the samples at different temperatures were measured, and the results are illustrated in Figure 8a–d. It is evident that all the $p\text{-}c\text{-}T$ curves of the samples exhibited only one flat desorption plateau at each temperature, indicating that only one phase, namely Mg/MgH_2 , is involved in the reversible hydrogenation cycling. The changes in enthalpy (ΔH) and entropy (ΔS) related to the hydrogen absorption and desorption reactions of the composites can be calculated using the van't Hoff equation [46]:

$$\ln \frac{p_{eq}}{p_0} = -\frac{\Delta H}{RT} + \frac{\Delta S}{R} \quad (3)$$

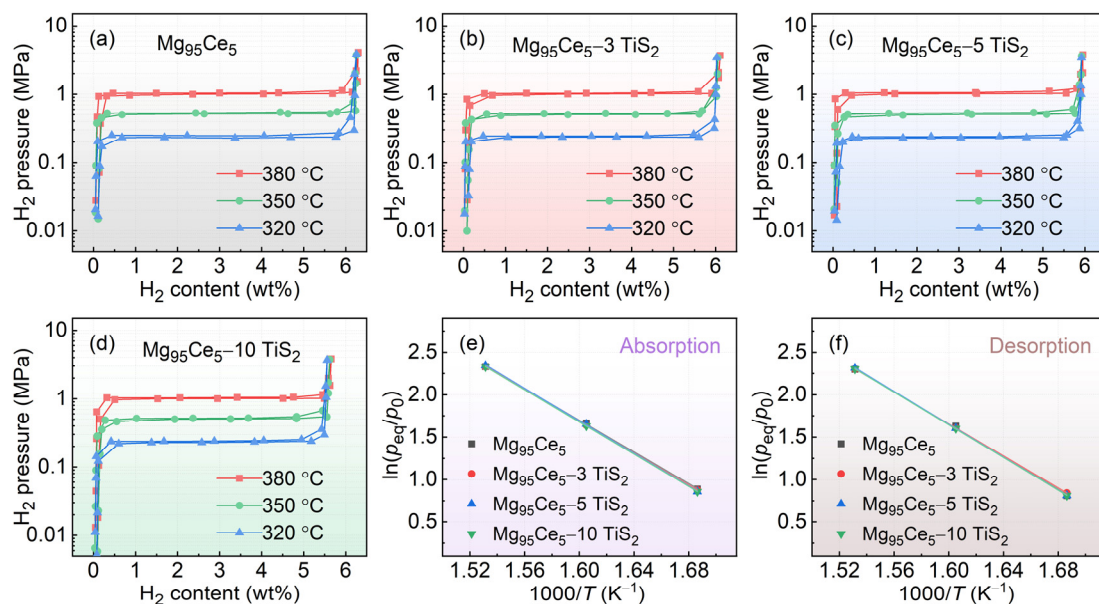


Figure 8. (a–d) $p\text{-}c\text{-}T$ curves of the $\text{Mg}_{95}\text{Ce}_5\text{-TiS}_2$ composites at different temperatures; (e,f) van't Hoff plots and corresponding fitting lines for hydrogen absorption and desorption reactions.

Here p_{eq} is the dehydrogenation equilibrium pressure (MPa), p_0 is the standard atmospheric pressure (0.101325 MPa), R represents the gas constant ($8.314 \text{ J mol}^{-1} \text{ K}^{-1}$), and T represents the experimental temperature (K). The van't Hoff plots for the hydrogenation and dehydrogenation reactions of the $\text{Mg}_{95}\text{Ce}_5\text{-TiS}_2$ composites are shown in Figure 8e,f, and the calculated ΔH and ΔS values are listed in Table 2. Notably, there is no significant difference in ΔH and ΔS values, indicating that the TiS_2 had little effect on the hydrogen absorption and desorption thermodynamic properties of $\text{Mg}_{95}\text{Ce}_5$ alloy. This is mainly because the de/re-hydrogenation reactions in the $\text{Mg}_{95}\text{Ce}_5\text{-TiS}_2$ composites were $\text{Mg} + \text{H}_2 \leftrightarrow \text{MgH}_2$, and the catalyst could not markedly affect the hydrogen absorption and desorption reaction process.

Table 2. Calculated ΔH and ΔS values for hydrogen absorption and desorption reactions of the Mg₉₅Ce₅–TiS₂ composites.

Samples	Absorption		Desorption	
	ΔH (kJ mol ⁻¹ H ₂)	ΔS (J K ⁻¹ mol ⁻¹ H ₂)	ΔH (kJ mol ⁻¹ H ₂)	ΔS (J K ⁻¹ mol ⁻¹ H ₂)
Mg ₉₅ Ce ₅	−77.5	−138.1	79.9	141.7
Mg ₉₅ Ce ₅ –3 TiS ₂	−78.1	−138.9	78.3	139.0
Mg ₉₅ Ce ₅ –5 TiS ₂	−79.8	−141.4	80.6	142.7
Mg ₉₅ Ce ₅ –10 TiS ₂	−78.9	−140.2	80.0	141.7

4. Conclusions

Mg₉₅Ce₅ alloy was prepared by vacuum induction melting, and then Mg₉₅Ce₅–TiS₂ composites with different TiS₂ contents were prepared through the mechanical ball-milling method. The XRD and SEM analysis results indicate that the Mg₉₅Ce₅ alloy was composed of CeMg₁₂ and Mg phases. The TiS₂ content had no effect on the phase compositions of the ball-milled Mg₉₅Ce₅–TiS₂ composites. The Mg₉₅Ce₅ alloy could be irreversibly hydrogenated into MgH₂ and CeH_{2.73} during the hydrogenation process, while the TiS₂ catalyst in Mg₉₅Ce₅–TiS₂ composites transformed into CeS₂ and TiH_{1.5}. The addition of TiS₂ significantly improved the hydrogen absorption and desorption kinetic performance of the Mg₉₅Ce₅. The dehydrogenation peak temperature of the Mg₉₅Ce₅ alloy could be reduced from 389.5 °C to 329.7 °C when the TiS₂ content was increased from 0 to 10 wt%. By comparison, the addition of TiS₂ had no impact on the hydrogenation and dehydrogenation thermodynamic parameters (ΔH and ΔS). It is certain that TiS₂ is an effective catalyst that can be used to enhance the hydrogen storage performance of magnesium-based materials.

Author Contributions: Methodology, X.O.; Software, L.W.; Validation, X.O.; Investigation, H.L. and X.O.; Resources, L.W.; Data curation, H.L.; Writing—review and editing, Z.L.; Supervision, X.O. and Z.L.; Project administration, Z.L.; Funding acquisition, X.O. All authors have read and agreed to the published version of the manuscript.

Funding: This research was funded by the Excellent Young and Middle-Aged Science and Technology Innovation Team Project in the Higher Education Institutions of Hubei Province (Grant No. T2020024), and the Fund for Hanjiang Normal University Key Subjects Construction.

Data Availability Statement: Data are contained within the article.

Conflicts of Interest: The authors declare no conflict of interest.

References

- Ahmed, S.; Irshad, M.; Yoon, W.; Karanwal, N.; Sugiarto, J.R.; Khan, M.K.; Kim, S.K.; Kim, J. Evaluation of MgO as a promoter for the hydrogenation of CO₂ to long-chain hydrocarbons over Fe-based catalysts. *Appl. Catal. B-Environ.* **2023**, *338*, 123052. [[CrossRef](#)]
- Ahmed, S.; Bibi, S.S.; Irshad, M.; Asif, M.; Khan, M.K.; Kim, J. Synthesis of long-chain paraffins over bimetallic Na–Fe_{0.9}Mg_{0.1}O_x by direct CO₂ hydrogenation. *Top. Catal.* **2024**, *67*, 363–376. [[CrossRef](#)]
- Hassan, Q.; Abdulateef, A.M.; Hafedh, S.A.; Al-samari, A.; Abdulateef, J.; Sameen, A.Z.; Salman, H.M.; Al-Jiboory, A.K.; Wieteska, S.; Jaszcjur, M. Renewable energy-to-green hydrogen: A review of main resources routes, processes and evaluation. *Int. J. Hydrogen Energy* **2023**, *48*, 17383–17408. [[CrossRef](#)]
- Shao, H.Y.; He, L.Q.; Lin, H.J.; Li, H.W. Progress and trends in magnesium-based materials for energy-storage research: A review. *Energy Technol.* **2017**, *5*, 445–458. [[CrossRef](#)]
- Jain, I.P.; Lal, C.; Jain, A. Hydrogen storage in Mg: A most promising material. *Int. J. Hydrogen Energy* **2010**, *35*, 5133–5144. [[CrossRef](#)]
- Zhang, L.C.; Zhang, X.; Zhang, W.X.; Huang, Z.G.; Fang, F.; Li, J.; Yang, L.; Gu, C.; Sun, W.; Gao, M.; et al. Nanoparticulate ZrNi: In situ disproportionation effectively enhances hydrogen cycling of MgH₂. *ACS Appl. Mater. Interfaces* **2023**, *15*, 40558–40568. [[CrossRef](#)]

7. Yang, T.; Yuan, Z.M.; Bu, W.G.; Jia, Z.C.; Qi, Y.; Zhang, Y.H. Evolution of the phase structure and hydrogen storage thermodynamics and kinetics of Mg₈₈Y₁₂ binary alloy. *Int. J. Hydrogen Energy* **2016**, *41*, 2689–2699. [[CrossRef](#)]
8. Yong, H.; Guo, S.H.; Yuan, Z.M.; Qi, Y.; Zhao, D.L.; Zhang, Y.H. Phase transformation, thermodynamics and kinetics property of Mg₉₀Ce₅RE₅ (RE = La, Ce, Nd) hydrogen storage alloys. *J. Mater. Sci. Technol.* **2020**, *51*, 84–93. [[CrossRef](#)]
9. Yong, H.; Wei, X.; Hu, J.F.; Yuan, Z.M.; Wu, M.; Zhao, D.L.; Zhang, Y. Influence of Fe@C composite catalyst on the hydrogen storage properties of Mg–Ce–Y based alloy. *Renew. Energ.* **2020**, *162*, 2153–2165. [[CrossRef](#)]
10. Wang, Z.X.; Tian, Z.H.; Yao, P.F.; Zhao, H.M.; Xia, C.Q.; Yang, T. Improved hydrogen storage kinetic properties of magnesium-based materials by adding Ni₂P. *Renew. Energ.* **2022**, *189*, 559–569. [[CrossRef](#)]
11. Tian, Z.H.; Wang, Z.X.; Yao, P.F.; Xia, C.Q.; Yang, T.; Li, Q. Hydrogen storage behaviors of magnesium hydride catalyzed by transition metal carbides. *Int. J. Hydrogen Energy* **2021**, *46*, 40203–40216. [[CrossRef](#)]
12. Meng, Q.F.; Huang, Y.Q.; Ye, J.K.; Xia, G.L.; Wang, G.F.; Dong, L.X.; Yang, Z.; Yu, X. Electrospun carbon nanofibers with in-situ encapsulated Ni nanoparticles as catalyst for enhanced hydrogen storage of MgH₂. *J. Alloys Compd.* **2021**, *851*, 156874. [[CrossRef](#)]
13. Ren, L.; Zhu, W.; Zhang, Q.U.; Lu, C.; Sun, F.Z.; Lin, X.; Zou, J. MgH₂ confinement in MOF-derived N-doped porous carbon nanofibers for enhanced hydrogen storage. *Chem. Eng. J.* **2022**, *434*, 134701. [[CrossRef](#)]
14. Liu, M.J.; Zhao, S.C.; Xiao, X.Z.; Chen, M.; Sun, C.H.; Yao, Z.D.; Hu, Z.; Chen, L. Novel 1D carbon nanotubes uniformly wrapped nanoscale MgH₂ for efficient hydrogen storage cycling performances with extreme high gravimetric and volumetric capacities. *Nano Energy* **2019**, *61*, 540–549. [[CrossRef](#)]
15. Wang, S.; Gao, M.X.; Yao, Z.H.; Xian, K.C.; Wu, M.H.; Liu, Y.F.; Sun, W.; Pan, H. High-loading, ultrafine Ni nanoparticles dispersed on porous hollow carbon nanospheres for fast (de)hydrogenation kinetics of MgH₂. *J. Magnes. Alloys* **2022**, *10*, 3354–3366. [[CrossRef](#)]
16. Xie, L.H.; Xu, M.; Zhang, C.; Wu, T. Composition dependent hydrogen storage performance and desorption factors of Mg–Ce based alloys. *Int. J. Hydrogen Energy* **2020**, *45*, 9865–9876. [[CrossRef](#)]
17. Yang, T.; Li, Q.; Liang, C.Y.; Wang, X.H.; Xia, C.Q.; Wang, H.S.; Yin, F.; Zhang, Y. Microstructure and hydrogen absorption/desorption properties of Mg₂₄Y₃M (M = Ni, Co, Cu, Al) alloys. *Int. J. Hydrogen Energy* **2018**, *43*, 8877–8887. [[CrossRef](#)]
18. Fu, Y.K.; Yu, Z.C.; Guo, S.Y.; Li, Y.; Peng, Q.M.; Zhang, L.; Wu, S.; Han, S. Catalytic effect of bamboo-like carbon nanotubes loaded with NiFe nanoparticles on hydrogen storage properties of MgH₂. *Chem. Eng. J.* **2023**, *458*, 141337. [[CrossRef](#)]
19. Czujko, T.; Varin, R.A.; Chiu, C.; Wronski, Z. Investigation of the hydrogen desorption properties of Mg + 10 wt.%X (X = V, Y, Zr) submicrocrystalline composites. *J. Alloys Compd.* **2006**, *414*, 240–247. [[CrossRef](#)]
20. Liang, G.; Huot, J.; Boily, S.; Van Neste, A.; Schulz, R. Catalytic effect of transition metals on hydrogen sorption in nanocrystalline ball milled MgH₂–Tm (Tm=Ti, V, Mn, Fe and Ni) systems. *J. Alloys Compd.* **1999**, *292*, 247–522. [[CrossRef](#)]
21. Shukla, V.; Yadav, T.P. Notable catalytic activity of CuO nanoparticles derived from metal-organic frameworks for improving the hydrogen sorption properties of MgH₂. *Int. J. Energy Res.* **2022**, *46*, 12804–12819. [[CrossRef](#)]
22. Dan, L.; Wang, H.; Yang, X.B.; Liu, J.W.; Ouyang, L.Z.; Zhu, M. Room-temperature transient hydrogen uptake of MgH₂ induced by Nb-doped TiO₂ solid-solution catalysts. *ACS Appl. Mater. Interfaces* **2023**, *15*, 30372–30382. [[CrossRef](#)] [[PubMed](#)]
23. Malka, I.E.; Pisarek, M.; Czujko, T.; Bystrzycki, J. A study of the ZrF₄, NbF₅, TaF₅, and TiCl₃ influences on the MgH₂ sorption properties. *Int. J. Hydrogen Energy* **2011**, *36*, 12909–12917. [[CrossRef](#)]
24. Grzech, A.; Lafont, U.; Magusin, P.C.M.M.; Mulder, F.M. Microscopic study of TiF₃ as hydrogen storage catalyst for MgH₂. *J. Phys. Chem. C* **2012**, *116*, 26027–26035. [[CrossRef](#)]
25. Lototskyy, M.; Sibanyoni, J.M.; Denys, R.V.; Williams, M.; Pollet, B.G.; Yartys, V.A. Magnesium–carbon hydrogen storage hybrid materials produced by reactive ball milling in hydrogen. *Carbon* **2013**, *57*, 146–160. [[CrossRef](#)]
26. Oelerich, W.; Klassen, T.; Bormann, R. Metal oxides as catalysts for improved hydrogen sorption in nanocrystalline Mg-based materials. *J. Alloys Compd.* **2001**, *315*, 237–242. [[CrossRef](#)]
27. Li, L.; Zhang, Z.C.; Jiao, L.F.; Yuan, H.T.; Wang, Y.J. In situ preparation of nanocrystalline Ni@C and its effect on hydrogen storage properties of MgH₂. *Int. J. Hydrogen Energy* **2016**, *41*, 18121–18129. [[CrossRef](#)]
28. Xie, W.J.; Liu, K.; Shi, G.D.; Fu, X.L.; Chen, X.J.; Fan, Z.X.; Liu, M.; Yuan, M.; Wang, M. CoS₂ nanowires supported graphdiyne for highly efficient hydrogen evolution reaction. *J. Energy Chem.* **2021**, *60*, 272–278. [[CrossRef](#)]
29. Wu, A.P.; Tian, C.G.; Jiao, Y.Q.; Yan, Q.; Yang, G.Y.; Fu, H.G. Sequential two-step hydrothermal growth of MoS₂/CdS core-shell heterojunctions for efficient visible light-driven photocatalytic H₂ evolution. *Appl. Catal. B-Environ.* **2017**, *203*, 955–963. [[CrossRef](#)]
30. Yuan, Z.M.; Zhang, Y.H.; Yang, T.; Bu, W.G.; Guo, S.H.; Zhao, D.L. Microstructure and enhanced gaseous hydrogen storage behavior of CoS₂-catalyzed Sm₅Mg₄₁ alloy. *Renew. Energ.* **2018**, *116*, 878–891. [[CrossRef](#)]
31. Yuan, Z.M.; Zhang, W.; Zhang, P.L.; Zhang, Y.H.; Bu, W.G.; Guo, S.H.; Zhao, D. Improvement in the hydrogen storage performance of as-milled Sm-Mg alloys using MoS₂ nano-particle catalysts. *RSC Adv.* **2017**, *7*, 56365–56374. [[CrossRef](#)]
32. Yuan, Z.M.; Zhang, W.; Zhang, Y.H.; Guo, S.H.; Dong, X.P.; Zhao, D.L. A comparison study of hydrogen storage properties of as-milled Sm₅Mg₄₁ alloy catalyzed by CoS₂ and MoS₂ nano-particles. *J. Mater. Sci. Technol.* **2018**, *34*, 1851–1858. [[CrossRef](#)]

33. Wang, P.; Wang, Z.X.; Tian, Z.H.; Xia, C.Q.; Yang, T.; Liang, C.Y.; Li, Q. Enhanced hydrogen absorption and desorption properties of MgH₂ with NiS₂: The catalytic effect of in-situ formed MgS and Mg₂NiH₄ phases. *Renew. Energ.* **2020**, *160*, 409–417. [CrossRef]
34. Liu, F.L.; Fang, L.Y.; Li, Z.Y.; Tan, Y.K.; Wang, J.; He, X.C.; Xu, G.; Ouyang, Y.; Tao, X. Diffusion behaviors and mechanical properties of binary Mg–Ce system. *Vacuum* **2023**, *216*, 112409. [CrossRef]
35. Jia, Y.; Guo, Y.N.; Zou, J.; Yao, X.D. Hydrogenation/dehydrogenation in MgH₂-activated carbon composites prepared by ball milling. *Int. J. Hydrogen Energy* **2012**, *37*, 7579–7585. [CrossRef]
36. Cho, Y.H.; Aminorroaya, S.; Liu, H.K.; Dahle, A.K. The effect of transition metals on hydrogen migration and catalysis in cast Mg–Ni alloys. *Int. J. Hydrogen Energy* **2011**, *36*, 4984–4992. [CrossRef]
37. Toè, S.D.; Russo, S.L.; Maddalena, A.; Principi, G.; Saber, A.; Sartori, S.; Spataru, T. Hydrogen desorption from magnesium hydride–graphite nanocomposites produced by ball milling. *Mat. Sci. Eng. B-Adv.* **2004**, *108*, 24–27. [CrossRef]
38. Ouyang, L.Z.; Huang, J.M.; Wang, H.; Wen, Y.J.; Zhang, Q.A.; Sun, D.L.; Zhu, M. Excellent hydrolysis performances of Mg₃RE hydrides. *Int. J. Hydrogen Energy* **2013**, *38*, 2973–2978. [CrossRef]
39. Yartys, V.A.; Gutfleisch, O.; Panasyuk, V.V.; Harris, I.R. Desorption characteristics of rare earth (R) hydrides (R=Y, Ce, Pr, Nd, Sm, Gd and Tb) in relation to the HDDR behaviour of R–Fe-based-compounds. *J. Alloys Compd.* **1997**, *253–254*, 128–133. [CrossRef]
40. Bhatnagar, A.; Johnson, J.K.; Shaz, M.A.; Srivastava, O.N. TiH₂ as a dynamic additive for improving the de/rehydrogenation properties of MgH₂: A combined experimental and theoretical mechanistic investigation. *J. Phys. Chem. C* **2018**, *122*, 21248–21261. [CrossRef]
41. Wu, C.Z.; Wang, P.; Yao, X.D.; Liu, C.; Chen, D.M.; Lu, G.Q.; Cheng, H. Effects of SWNT and metallic catalyst on hydrogen absorption/desorption performance of MgH₂. *J. Phys. Chem. B* **2005**, *109*, 22217–22221. [CrossRef] [PubMed]
42. Chen, M.; Hu, M.M.; Xie, X.B.; Liu, T. High loading nanoconfinement of V-decorated Mg with 1 nm carbon shells: Hydrogen storage properties and catalytic mechanism. *Nanoscale* **2019**, *11*, 10045–10055. [CrossRef]
43. Ji, L.; Zhang, L.; Yang, X.; Zhu, X.; Chen, L. The remarkably improved hydrogen storage performance of MgH₂ by the synergetic effect of an FeNi/rGO nanocomposite. *Dalton T.* **2020**, *49*, 4146–4154. [CrossRef]
44. Ren, L.; Zhu, W.; Li, Y.H.; Lin, X.; Xu, H.; Sun, F.Z.; Lu, C. Oxygen vacancy-rich 2D TiO₂ nanosheets: A bridge toward high stability and rapid hydrogen storage kinetics of nano-confined MgH₂. *Nano-Micro Lett.* **2022**, *14*, 144. [CrossRef]
45. Li, X.J.; Fu, Y.K.; Xie, Y.C.; Cong, L.; Yu, H.; Zhang, L.; Li, Y.; Han, S. Effect of Ni/tubular g-C₃N₄ on hydrogen storage properties of MgH₂. *Int. J. Hydrogen Energy* **2021**, *46*, 33186–33196. [CrossRef]
46. Schlapbach, L.; Züttel, A. Hydrogen-storage materials for mobile applications. *Nature* **2001**, *414*, 353–358. [CrossRef]

Disclaimer/Publisher’s Note: The statements, opinions and data contained in all publications are solely those of the individual author(s) and contributor(s) and not of MDPI and/or the editor(s). MDPI and/or the editor(s) disclaim responsibility for any injury to people or property resulting from any ideas, methods, instructions or products referred to in the content.